Review

# Recent Progress on Semi-transparent Perovskite Solar Cell for Building-integrated Photovoltaics

ZHU Yiyi[1,2], SHU Lei[1,2] and FAN Zhiyong[1,2*]

*1. HKUST-Shenzhen Research Institute, Shenzhen 518057, P. R. China;*

*2. Department of Electronic and Computer Engineering, Hong Kong University of Science and Technology(HKUST),
Clear Water Bay, Kowloon, Hong Kong SAR, P. R. China*

**Abstract**   The electricity consumption of buildings is tremendous; moreover, a huge amount of electricity is lost during distribution. Taking away this consumption can significantly reduce energy demand and greenhouse effect gas emission. One of the low-cost and renewable solutions to this issue is to install photovoltaic panels on the buildings themselves, namely, building-integrated photovoltaics(BIPVs). Using this technology, power generation roofs, windows, and facades can harvest solar radiation and convert to electricity for building power consumption. Semi-transparent perovskite solar cells(ST-PSCs) have attracted tremendous attention for the power generation windows, due to the excellent photoelectric properties, versatile fabrication methods, bandgap tunability, and flexibility. Here, an overview is provided on the recent progress of ST-PSCs for BIPV, which mainly focuses on the control of perovskite morphology, optical engineering for an efficient and semi-transparent ST-PSC. We also summarize recent development on various transparent electrodes and present prospects and challenges for the commercialization of ST-PSCs.

**Keywords**   Building-integrated photovoltaic; Semi-transparent solar cell; Perovskites solar cell

## 1   Introduction

Fast global urbanization and environmental pollution have provoked a search for an eco-friendly source of renewable energy. Solar energy is the most abundant sustainable energy in the world. Whereas, due to the relatively high cost, the widespread photovoltaic installation was hindered. In 2018 photovoltaic technologies only stood for 3% of the worldwide total energy demand[1]. According to the commercial buildings energy consumption survey in 2016, the total annual electricity consumption of buildings in the United States is 25 TWh, which accounts for nearly 40% of the total energy demand[2]. Taking away this consumption can significantly reduce energy demand and environmental pollution.

Green buildings should design along with a sustainable principle so that it can produce all the energies it needs by itself. Currently, the dominant product for building-integrated photovoltaics(BIPVs) in the market is opaque silicon solar cells. The opaque photovoltaics modules, which can only be mounted at the limited rooftop, is not a  desirable solution in densely packed cities[3]. Still, it has the potential to cover 38.6% of the total electricity generation in the United States. In contrast, the power generation windows in buildings are assumed to be a practical solution to reach the ultimate target of self-sustaining buildings in cities. Because the electricity generated by the

newly emerged semi-transparent photovoltaic device(ST-PV) integrated on facades, windows, skylights of commercial and residential buildings is enormous compared with rooftop photovoltaic modules[2,4,5].

The newly emerged organic-inorganic perovskite(PVSK) is a promising candidate as the photon absorber of ST-PV. Over the past few years, the progress of power conversion efficiency(PVSK) has been boosted at an unprecedented rate in terms of power conversion efficiency(PCE), device longevity and less toxicity[6,7]. The efficiency has reached a record high of 25.2%(certified) in 2019[8]. However, considering its application in the power generation windows, the toxicity, and stability issues associated with PVSK are the main concerns before its real-life application. Luckily, the long-term stability of PVSK has been significantly improved through strategies, such as the defects passivation, PVSK composition modification, etc.[9]. A lifetime of 10000 h was achieved for perovskite solar cells(PSCs) under continuous one sun AM 1.5 G illumination at an elevated temperature of 55 °C[10]. Another attractive feature is the ability to tune its bandgap from 1.48 eV to 2.3 eV[11—13], which indicates the possibility of colorful ST-PSCs. Besides, the low-temperature processability of PVSK offers the potential of large-scale manufacture of cost-effective solar cells with a short energy payback time.

Here, we provide an overview of the recent development

---

in ST-PSC for BIPV, which mainly focuses on the control of PVSK morphology and optical engineering for an efficient semi-transparent PVSK. This includes the ultra-thin light active layer, micro island-type structures, and nanostructure PVSK. We also summarise the recent progress of transparent and conductive top and bottom electrodes. In the end, we present prospects and challenges for the commercialization of ST-PSCs.

## 2   Semitransparent PVSKs

Unlike conventional photovoltaic products, which are mainly evaluated by PCE, ST-PV should harvest enough solar radiation and convert it to electricity for building consumption. On the other hand, they need to transmit a certain port of daylight to illuminate indoor space. Therefore, the trade-off between the electricity generation and light transmittance requirements should be balanced for ST-PV. The transparency of solar cells can be improved by reducing the thickness or surface coverage of the light-active layer. However, these strategies will lead to a sacrifice of device PCE ultimately.

The recognition of the human eyes is different from the spectrometer. The light scattering from a rough surface will cause less visual transparency to the human eyes, even though the transparency measured in the spectrometer is high. Moreover, from the luminosity of human perception shown in Fig.1(A), human eyes are sensitive to green light($\lambda$=550 nm) but less sensitive in the blue and red ranges[14]. Harvesting photons in those less sensitive regions is a feasible way to achieve high visual transparent ST-PSCs without compromising efficiency. Therefore, in order to achieve high visual transparency, the light scattering from a rough surface, and the human luminosity factor should be taken into consideration.

There are a few figure-of-merits for transparency of ST-PSCs; for instance, average visible transmittance(AVT), luminosity, and optical scattering[15]. AVT is the most commonly used index. Demonstrated in Eq.(1), AVT can be determined by the average transparency in the visible wavelength range(400—760 nm) based on the photopic response of the human eyes. Though the requirement of AVT is determined by its application, in general, an ST-PSC with AVT of 20%—30% is already acceptable for the power generation windows[16]. The luminosity is human visual sensitivity to light; the

corresponding curve of luminosity is shown in Fig.1(A).

$$AVT = \frac{\int T(\lambda)P(\lambda)S(\lambda)d\lambda}{\int P(\lambda)S(\lambda)d\lambda} \tag{1}$$

$$Luminosity = \frac{\int T(\lambda)P(\lambda)d\lambda}{\int P(\lambda)d\lambda} \tag{2}$$

wherein, $\lambda$ is the wavelength, $S(\lambda)$ is the solar energy flux (AM1.5 100 MW/cm$^2$) at $\lambda$, $T(\lambda)$ is the transmittance at $\lambda$, $P(\lambda)$ is the photopic response of human eyes at $\lambda$.

Generally, the ST-PV with a neutral color is favorable for the majority power generation windows, which allows for occupants to link to the outsides. However, sometimes it is preferred to have ST-PV with different colors with decorative purposes.The Commission International de L'Eclairage(CIE) 1931 chromaticity diagram is a widely adopted method to evaluate human visual color perception. Fig.1(B) and (C) show the CIE *XYZ* standard observer color matching functions and the CIE 1931 color space chromaticity diagram, respectively. The tristimulus values(*X, Y, Z*) and the color coordinates(*x, y, z*) were calculated from the device transmittance spectra, using the following formula[17]:

$$X = \int_{380\,nm}^{780\,nm} S(\lambda) \times \bar{x}(\lambda) \times T(\lambda)d\lambda \tag{3}$$

$$Y = \int_{380\,nm}^{780\,nm} S(\lambda) \times \bar{y}(\lambda) \times T(\lambda)d\lambda \tag{4}$$

$$Z = \int_{380\,nm}^{780\,nm} S(\lambda) \times \bar{z}(\lambda) \times T(\lambda)d\lambda \tag{5}$$

$$x = \frac{X}{X + Y + Z} \tag{6}$$

$$y = \frac{Y}{X + Y + Z} \tag{7}$$

$$z = \frac{Z}{X + Y + Z} \tag{8}$$

wherein $\bar{x}(\lambda)$, $\bar{y}(\lambda)$, $\bar{z}(\lambda)$ are the standard observer color matching functions.

Colorful PSCs have been achieved through several strategies, such as the modification of PVSK morphology[18], integration of a porous photonic crystals scaffold[19], incorporations of plasmonic color filters[20], and deposition of luminescent down-shifting layers[21]. Most widely reported colorful ST-PSCs are realized by tuning the bandgap($E_g$) of PVSK. With
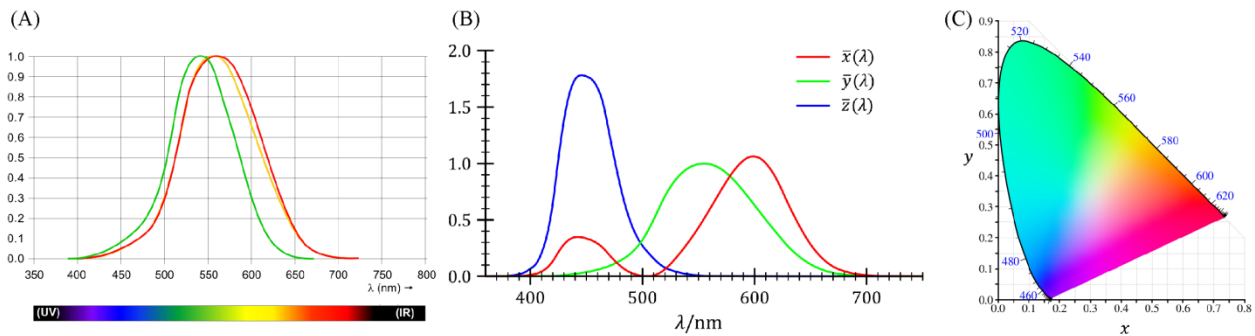


**Fig.1    Protanopic(green) and deuteranopic(red) luminosity functions(A)(for comparison, the standard photopic curve is shown in yellow), the CIE *XYZ* standard observer color matching functions(B) and the CIE 1931 color space chromaticity diagram(C)**
(A) Reprinted with permission from ref. [14].

the formulation of $ABX_3$, the bandgap of PVSK can be easily tuned by managing elements at positions of A [methylammonium(MA) or formamidinium(FA) and caesium (Cs) cation] with B being lead(Pb), tin(Sn), and $X$ being a halide(I, Br, or Cl). The substitution of I with Br increases the $E_g$ of mixed halide PVSK, which leads to a color tunability from dark brown to yellow. Take $CsPb[I_{(1-x)}Br_x]_3$, $MAPb[I_{(1-x)}Br_x]_3$, $FAPb[I_{(1-x)}Br_x]_3$ for example, the $E_g$ increased from 1.73 eV to 2.38 eV [22], 1.58 eV to 2.28 eV[12], and 1.48 eV to 2.3 eV[23], respectively, with improving the Br concentration. Besides, slightly replacing FA or MA with inorganic Cs cation results in a PVSK with a bandgap shift and a better moisture-tolerance[24].

In this section, we have summarized recent strategies toward efficient ST-PSCs, for instance, ultra-thin active layers, and decreasing surface coverage of PVSK by the formation of micro island-type structures and nanostructure PVSK. Moreover, the performances of ST-PSC *via* different approaches were discussed.

## 2.1 Ultrathin Active Layers

Obtaining a continuous ultrathin PVSK layer is a common and practical approach for achieving an efficient ST-PSC[25—31]. The tunable transparency of PVSK thin-film can be obtained by controlling its thickness, which was realized by the spin-coating method with low concentration precursor solution[30] and vacuum thermal evaporation technique. The surface roughness plays a vital role in the visual transparency of PVSK thin-film, as the light scattering can be suppressed by the formation of the ultra-smooth top surface of PVSK thin-film[32,33]. Besides, to achieve a high $V_{oc}$ and high shunt resistance, a compact thin-film without any pin-hole is required. Therefore, it is feasible to achieve an efficient ST-PSC with high visual transparency through the optimization for a smooth and pin-hole free PVSK thin-film.

However, the ST-PSCs based on ultrathin PVSK suffer from the optical appearance of reddish-brown and cannot realize the desired neutral color ST-PSCs. This can be ascribed to the traps states near the conduction band minimum and valence band maximum in the polycrystalline PVSK. As a result, its absorption coefficient increased monotonically from the bandgap.

Ono *et al.*[26] achieved ST-PSCs with a PCE of 9.9% ($V_{oc}$=1.09 V) based on PVSK thin-film with a thickness of 135 nm. You *et al.*[31] fabricated continuous PVSK thin-films with thickness ranging from 150 nm to 350 nm through a one-step spin-coating method. To achieve ST-PSCs with high visual transparency, Kim *et al.*[33] fabricated an ultra-smooth PVSK thin film through a spin-coating method in combination with vacuum drying. The low roughness PVSK thin film(<6 nm) suppresses the light scattering to the point less than 2%. Thereafter, to improve the performance of ST-PSCs, Jung *et al.*[27] tried to optimize the energy band diagram by replacing the commonly-used hole transport layer(HTL) poly(3,4-ethylene-dioxythiophene):poly(styrene sulfonate)(PEDOT:PSS) with copper thiocyanate(CuSCN). As a result, the potential energy

loss at the interface between PVSK and HTL was reduced. The corresponding energy band diagram was demonstrated in Fig.2(A). The performance was significantly improved *via* interface engineering. The efficiency of the opaque device improved from 12.1%(the control PEDOT: PSS-based one) to 16.0%(CuSCN-based device). Furthermore, demonstrated in the Table 1, by increasing the thickness of PVSK thin-film, the PCEs of their ST-PSCs were boosted from 7.33% to 10.06% with a tunable AVT of the device varying between 37.5% and 13.0%. Notably, a record high $V_{oc}$ of 1.07 V for an ST-PSC was achieved. Shown in Fig.2(B), however, the transmittance of PVSK thin-film increased monotonically from the bandgap. The inset photograph of a semi-transparent device shows a brownish color appearance. To quantify the color properties of ST-PSCs, the corresponding color coordinates on CIE 1931 are illustrated in Fig.2(C). The color coordinates based on PVSK with different thicknesses(140, 180, and 240 nm) are (0.451, 0.398), (0.457, 0.403), and (0.468, 0.416), respectively, which needs further optimization to achieve a neutral color cell.

Despite that the success fabrication of ST-PSCs is based on ultrathin active layers through the solution process, the manufacture of large-area PVSK continuous thin-films remains challenging, which hinders its further practical implementation. In fact, the evaporation method is a cost-effective method for mass production[34—37]. For instance, a centimeter- scale PSC(5 cm×5 cm) with a PCE of 9.9% was already obtained through thermal evaporation[26]. Moreover, the flexibility of transparency and efficiency management can be realized by controlling the thickness of PVSK during vacuum thermal evaporation[38]. Reported by Roldán-Carmona *et al.*[38], with the thickness of PVSK varied from 40 nm to 280 nm, the average visible transmission of the active layer(AL-AVT) reduced from 45% to 19%, whereas the device PCE based on this thin-film boosted from 3.39% to 7.73%. After that, Chen *et al.*[39] reported the use of a dual-source vacuum evaporation method to fabricate high-quality $CsPbBr_3$ thin films. A record-high PCE of 7.78% for a $CsPbBr_3$-based planar PSC was reported. The cross-section SEM image of the $CsPbBr_3$-based PSCs is shown in the Fig.2(D). The $CsPbBr_3$ thin film demonstrates semi-transparent property and completely UV light blocking. Shown in Fig.2(E), the average visible transmittance of $CsPbBr_3$ thin-film reaches up to 90.9% for visible light in the range from 530 nm to 800 nm. Apart from the excellent optical properties, the $CsPbBr_3$ based device demonstrated impressive photostability against the UV-light irradiation, which means it is a promising candidate for the top cell of the tandem device[38,39]. Therefore, Chen *et al.*[39] fabricated four-terminal tandem solar cell with a top cell of the $CsPbBr_3$-based PSCs and a bottom cell of an organic solar cell, with the corresponding external quantum efficiency(EQE) spectra illustrated in Fig.2(F).

## 2.2 Micro Island-type Structures

Compared with the reddish-brown PVSK thin film, the microstructure PVSK exhibits a color-neutrality, which is preferred for the power generation windows. There are two
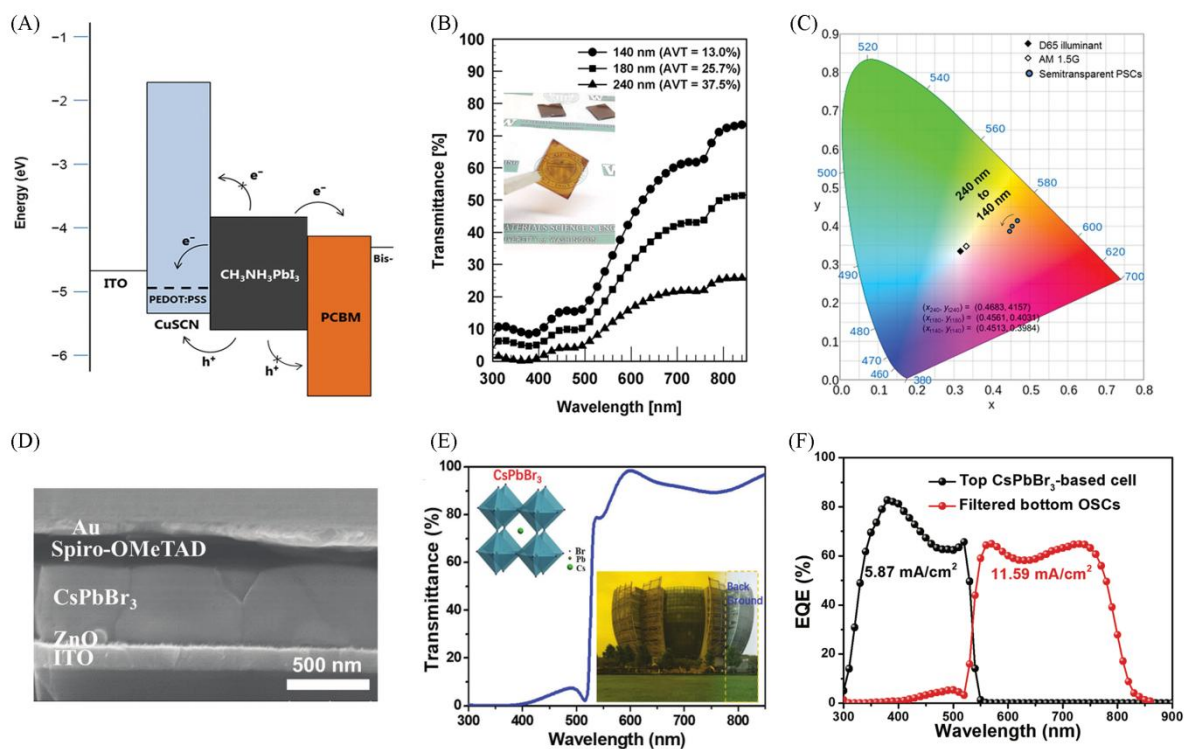
**Fig.2   Corresponding energy band diagram relative to vacuum level(A), UV-Vis transmittance of the semitransparent PVSC devices with different thicknesses of perovskite layer(inset is a photograph of a semitransparent PVSC device with a perovskite layer of 180 nm in thickness)(B), the representation of color coordinate of the semitransparent PHJ PVSCs with different thicknesses of perovskite layer on CIE 1931 chromaticity diagram(C), cross-section SEM image of a PSCs with the structure of glass/ITO/ZnO/CsPbBr$_3$/spiro-OMeTAD/Au(D), transmittance of the vacuum-evaporated 450 nm thick CsPbBr$_3$ film(inset: crystal structure of the CsPbBr$_3$ film and photograph of the library at Soochow University, taken through a vacuum-evaporated CsPbBr$_3$ film)(E) and EQE spectra of a CsPbBr$_3$-based top semitransparent solar cell and a bottom the organic solar cells(F)**

(A)—(C) Reprinted with permission from ref.[27]. Copyright 2015 Wiley-VCH; (D)—(F) reprinted with permission from ref.[39]. Copyright 2018, Wiley-VCH.

suggested approaches, including the partial dewetting of the substrate and the use of a honey comb-shaped oxide template.

The strategy towards ST-PSCs with the neutral transmission of light was proposed by Eperon *et al.*[40]. As shown in Fig.3(A) and (B), the light active layer based on microstructure PVSK "islands" was successfully fabricated by partial dewetting the substrate. The photo of the PVSK is shown in Fig.3(C); the grain size of PVSK "islands" is small enough to appear continuous to the human eyes, but large enough to enable the light transmission between two neighboring PVSK islands. The transparency of PVSK film can be controlled from close to 0 to 80% by changing the surface coverage. Notably, due to the adequate thickness of microstructure PVSK, most visible light was absorbed by the PVSK layer. This results in a neutral-colored PVSK. To evaluate the color-neutrality of ST-PSCs, the corresponding color coordinates on CIE 1931 are displayed in Fig.3(D).

Later on, Eperon *et al.*[41] tried to replace the MAI with FAI and achieved a more efficient ST-PSC based on similar microstructure PVSK. The device architecture diagram is shown in Fig.3(E). And the tilted and cross-sectional SEM images of the device are shown in Fig.3(F) and (G), respectively. Both the FA-based device and MA-based device demonstrate a neutral-colored semitransparent. Notably, shown in Table 1, such an FA-based device shows a PCE of over 5% at AL-AVT of almost 30%. As demonstrated in the *J-V* characteristics of MA- and FA-based devices[Fig.3(H)], the FA-based device(PCE=7.4%, AL-AVT=33.6%) demonstrates a higher efficiency and suppressed hysteresis behavior compared with an equivalent MA-based device(PCE=4.9%, AL-AVT=40.5%). Moreover, as shown in Fig.3(I), the angular dependence of photocurrent suggests that microstructure PVSK based devices possesses excellent performance at non-normal angles, which is superior to the commercial silicon solar cell. The excellent performance at high incident angles can be attributed to the light absorption by the edges of the PVSK islands. Despite the success fabrication of ST-PSC with color-neutrality, the photovoltaic performance of this microstructure PVSK[40,41] is much lower than that of the typical ST-PSCs based on a continuous thin film(Table 1)[26,31,42]. This can be ascribed to the incomplete coverage of PVSK on a substrate in microscale. The presence of regions that electron transport layer(ETL) and HTL directly contact causes the formation of a "shunt resistance" which leads to a loss of $V_{oc}$[43].

To suppress the undesired effect come along with the electronic contact of the HTL and ETL , Hörantner *et al.*[43]
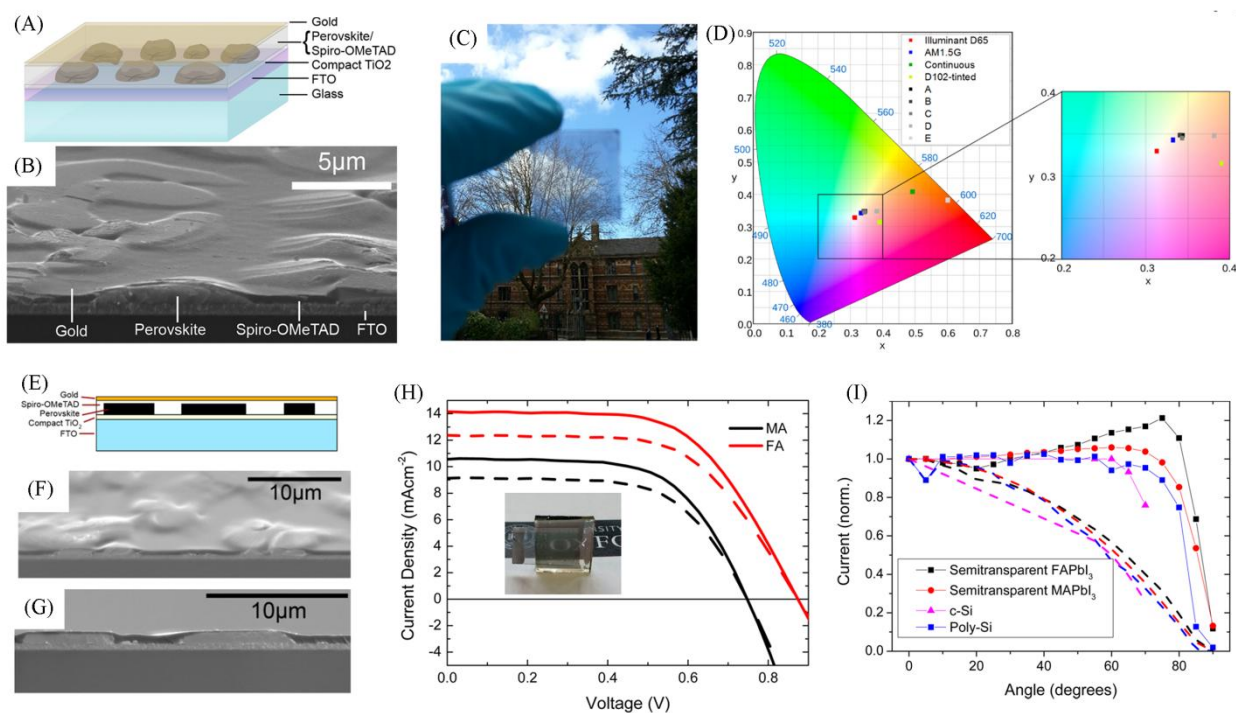
**Fig.3    Semi-transparent neutral-colored perovskite solar cells**

(A) Diagram showing the architecture of the dewetting planar perovskite heterojunction solar cell; (B) tilted cross-sectional SEM image of a full semitransparent solar cell showing the perovskite islands coated with spiro-OMeTAD; (C) photograph through a typical semitransparent perovskite film formed on glass, demonstrating neutral color and semitransparency; (D) color coordinates of the films on the CIE *xy* 1931 chromacity diagram, and the enlarged central region. Color coordinates of a thin continuous perovskite film, a D102 dye-tinted cell(perovskite+ D102/spiro-OMeTAD, 5 mg/mL indolene dye termed D102 in spiro-OMeTAD), the D65 standard daylight illuminant, and AM1.5 illumination are also shown; (E) diagram of the device architecture employed; tilted(F) and cross-sectional(G) SEM images of a full semitransparent $FAPbI_3$ solar cell showing the islands of perovskite coated with spiro-OMeTAD; (H) *J-V* characteristics of $MAPbI_3$ and $FAPbI_3$ solar cells, measured under simulated 100 mW·cm$^{-2}$ AM1.5 illumination, for both the measured data(solid lines) and that calculated for just one light pass(dashed lines)(inset is a photograph of a fully semitransparent FAPbI3 device including the laminated transparent cathode); (I) angle-dependent photocurrent extracted from $FAPbI_3$ and $MAPbI_3$ semitransparent solar cells, compared to that extracted from crystalline silicon(c-Si) and polycrystalline silicon(poly-Si) devices. 0° represents light incident at the normal; light incident at 90° is coming completely from the side of the device. Dashed lines take into account the reduced footprint of the solar cell with an increased illumination angle to represent the power output from a module in operation. (A)—(D) Reprinted with permission from ref.[40]. Copyright 2013 American Chemical Society; (E)—(I) reprinted with permission from ref.[41]. Copyright 2014 American Chemical Society.

reported the use of colloidal monolayer lithography to introduce a highly ordered honeycomb structure into the PVSK. Due to the honeycomb scaffold, the regions that directly contact HTL and ETL were suppressed. This results in the reddish-brown ST-PSCs with an AL-AVT of around 37%. Notably, shown in Table 1, compared with the control device, the pattern PVSK device demonstrated a higher $V_{oc}$ and FF. The ordered microstructure PVSK based ST-PSCs achieved a record high PCE of 9% with relatively high AL-AVT of 37%. However, the optical scatte- ring from the rough surface of a light-absorber will lead to poor visual transparency to the human eyes, even though the transmittance measured is high[43]. Hörantner *et al.*[43] believed the future work can be the optimization of template pore size and the distribution to suppress the light scatte- ring from the rough surface of PVSK.

After that, Zhang *et al.*[44] proposed the use of $SiO_2$ honeycomb structure to pattern a highly-ordered microstructure PVSK thin-film. First, large-scale monolayer colloidal crystals were fabricated by colloidal self-assembly[45]. Then, the polystyrene shell was precisely removed layer-by-layer *via* $O_2$ plasma etching[46]. Thus the diameter of microspheres can be controlled by varying $O_2$ plasma etching time. After the infiltration of the PVSK precursor solution, $SiO_2$ honeycomb structure patterned PVSK was obtained. As a result, a near-neutral-colored semitransparent PVSK film with 38% AL-AVT was achieved. ST-PSCs based on these demonstrated a record high PCE of 10.3%($V_{oc}$=0.98 V).

## 2.3   Nanostructure PVSK

Along with the development of ST-PSCs, the transmittance of PVSK has been successfully enhanced *via* the methods mentioned above. However, these methods inevitably result in a loss of PCE. To improve visual transparency without sacrifice the overall performance of solar cells, the light scattering and human luminosity factor[47] should be taken into account.

In contrast to unfavorable optical scattering from microstructure PVSK, the nanoscale structure can smooth the surface, which results in good visual transparency. Moreover, nanoengineering templates were proved to be an effective way to stabilize the cubic black phase of PVSK[48—51]. The anodized aluminum oxide(AAO) was employed as a scaffold layer to achieve a 1D nanostructured semitransparent PVSK[52].

Impressively, as shown in Fig.4(A) and (B), the transparency of PVSK can be precisely controlled by varying the AAO pore size and height. Moreover, with the introduction of a transparent cathodic electrode, which combined with indium tin oxide with a buffer layer($MoO_x$), a high-performance ST-PSC is obtained with a PCE of 9.6% and a whole device AVT of 33.4%. Notably, verified in impedance spectroscopy analyses [Fig.4(D)], internal ion diffusion was significantly suppressed. As a result, as demonstrated in Fig.4(E), the AAO scaffold layer-based, nanopillar structured PVSK solar cell has no hysteresis behavior. Moreover, due to the self-packing of AAO, the long-term stability of the device under continuous illumination was improved.

As shown in Fig.4(F), human luminosity is different for a photon with different wavelengths[47]. Therefore, harvesting photons in those less sensitive regions is a feasible way to achieve high visual transparent ST-PSCs without compromising efficiency. Concept of the visual transparency enhancement for ST-PSCs by considering the human luminosity factor was proposed by Kim *et al.*[47]. The ST-PSCs harvesting photons in the less sensitive blue and red ranges were fabricated. Shown in Fig.4(F) and (G), plasmonic silver nanotubes were utilized to improve the absorption of the photon in the red and deep-red ranges. The enhancement of red-light absorption was attributed to the plasmon coupling between transparent electrode and silver nanotubes[53—55]. On the other hand, as demonstrated in Fig.4(F) the light absorption of $MAPbI_3$ is higher at a short wavelength. Therefore, ST-PSCs harvesting lights in blue and red ranges were achieved. With a result, their strategy remarkably improved the performance of ST-PSCs, in terms of PCE, whole device AVT. When PCE is 9.73%, the whole device AVT reaches 17.8 for the deivce with $PCBM/AgNCs/BCP/Ag/MoO_3$, and when PCE is 9.18%, the whole device AVT reaches 15.2 for the controlled group.
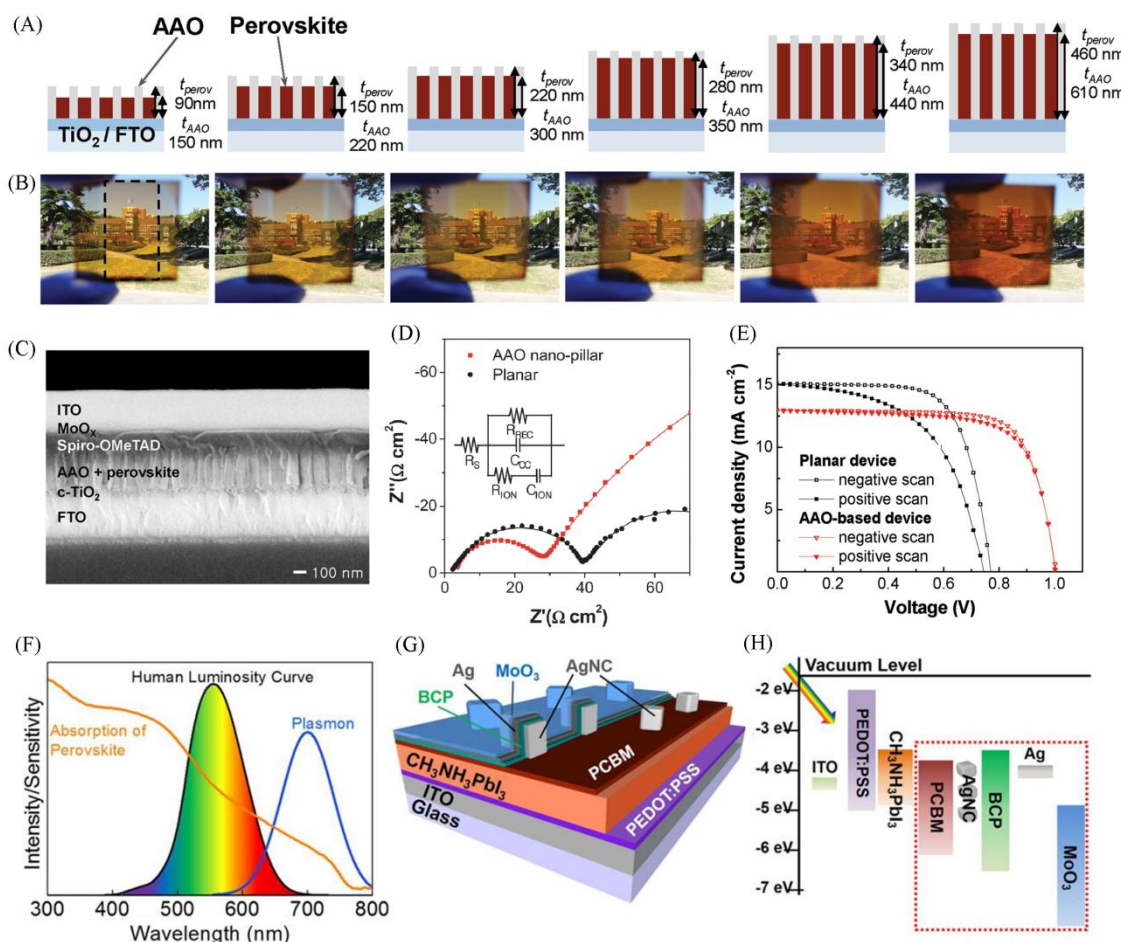


**Fig.4 Performance of nanopillar-structured perovskite devices with different AAO template/ perovskite layer thicknesses**

(A) Schematic showing spin-infiltrated perovskite layers in AAO templates with thicknesses of 150, 220, 300, 350, 440, and 610 nm; (B) pictures of the nanopillar-structured perovskite devices with different AAO template/perovskite layer thicknesses(prepared without Au cathode). The dotted line in the first picture indicates the area where the AAO template exists(active area); (C) cross-sectional SEM image of a nanopillar-structured perovskite solar cell with an ITO cathode and a thickness of $t_{PVSK}=280/t_{AAO}=350$; (D) Nyquist plots for spin-coated planar and spin-infiltrated nanopillar-structured perovskite cells, measured under 1 sun illumination with an applied forward DC bias of 0.4 V; (E) *J-V* curves for the two devices as a function of scan direction: positive($J_{sc}\rightarrow V_{oc}$) and negative($V_{oc}\rightarrow J_{sc}$). Both samples described here are composed of perovskite layers with nearly the same thickness($\approx$150 nm); (F) concept of the visual transparency improvement of the semi-transparent solar cells by considering the human luminosity curve; the structure(G) and the energy diagram(H) of PVSCs with electrode-coupled plasmons(ECPs). (A)—(E) Reprinted with permission from ref.[52]. Copyright 2016, Wiley-VCH; (F)—(H) Reprinted with permission from ref.[47]. Copyright 2017, Nature Publishing Group.

:

# 3 Transparent Electrode for ST-PSCs

Another challenge for an efficient ST-PSC is engineering the electrode maximum transparency, which has been extensively studied for years to transmit enough light without compromising charge collection. Shown in Table 1, the transparent conductive oxides(TCOs), including indium tin oxide(ITO)[56], fluorine-doped tin oxide(FTO)[57,58], indium-doped zinc oxide[59—61], and aluminum-doped zinc oxides[62,63], have been widely utilized as a bottom electrode for solar cell, due to their excellent transparency, low sheet resistance($R_s$=5—20 Ω/sq), effective charge collecting and robust stability.

However, the requirements for the top electrode of ST-PSCs are more critical. Apart from the excellent electrical and optical properties, the work function and deposition method are vital for achieving a high-performance solar cell. Few works have utilized TCOs as top electrodes, the main constraint stems from the damage of soft PVSK layer by the magnetron sputtering of TCOs[63]. Even though, people tried to avoid this damage by incorporating a protecting layer between PVSK and TCOs[58,64], the mainstream transparent and conductive materials for the top electrode are thin metal layers(Au[38], Ag[65]), carbon materials[25,66—68], metallic nanowires[30,69] and dielectric-metal-dielectric(DMD) multilayer[6,70].

## 3.1 Ultrathin Metal Film

The ultrathin metal film is a cost-effective material for large-area production. But there is a trade-off between transparency and conductivity for the ultrathin metal film top electrode. The morphology of metal thin film gradually changed from a continuous thin film to an island structure, as the thickness of the metal thin film decreased. As a result, the resistance of metal thin film will increase. Roldán-Cormona et al.[38] fabricated ST-PSCs by thermal evaporation of PVSK and ultrathin Au top electrode, which showed an average PCE of ca. 7%. Bryant et al.[57] fabricated ST-PSCs with Ni mesh top electrodes and FTO bottom electrodes and achieved a PCE of 13.3%.

## 3.2 Carbon Material

Carbon materials, for instance carbon nanotubes(CNTs) and graphene, are considered as a promising candidate for the top-electrode of ST-PSCs, thanks to the mechanical and chemical robustness, flexibility and the potential for mass-manufacture[71,72].

Graphene is widely used conductivity materials for transparent electrodes with flexible characteristics[64,73,74]. Tran et al.[75] first reported the fabrication of ST-PSCs by using the transfer free and large-area monolayer graphene as the top electrode. Moreover, owing to the excellent mechanical flexibility of graphene, their devices maintained >90% initial PCE after 1000 cycles bending. You et al.[31] first reported the fabrication of ST-PSCs by using the multiple layer graphene as the top transparent electrodes. Moreover, the conductivity of graphene can be dramatically improved by deposition a thin layer of poly-(3,4-ethylenedioxythiophene):poly(styrenesulfonate) (PEDOT:PSS) on graphene[76]. Li et al.[77] reported the use of a layer of carbon nanotubes networks to replace the organic hole transport layer and metal contact on ST-PSCs.

## 3.3 Metallic Nanowires

Despite the robust stability, mechanical flexibility, and potentially low cost, the sheet resistances for carbon materials are still too high(60—400 Ω/sq for CNT and 30—1000 Ω/sq for graphene)[78,79]. This leads to a low fill factor and poor performance for a solar cell. Metallic nanowires, which are solution-processable transparent electrodes, possess a higher electrical conductivity compared with the carbon materials[71,80]. Taken Ag nanowires(NWs) for example, sheet resistances can reach as low as 10—100 Ω/sq[81].

However, Ag-based transparent electrodes cause the degradation of PVSK because of the chemical reaction of sliver and halide[82]. In order to prevent this degradation, Guo et al.[28] incorporated a tunneling layer of ZnO nanoparticles at the interface between [6,6]-phenyl-C61-butyric acid methyl ester (PC$_{60}$BM) and AgNWs. Furthermore, the introduction of ZnO nanoparticles leads to better ohmic contact in the cell. Similarly, Han et al.[83] used the spin-coating method to deposit a layer of ZnO nanoparticles on the AgNWs electrode to improve the interconnection of AgNWs, which led to a boost of PCE from 7.31% to 11.13%.

## 3.4 Dielectric-metal-dielectric Stacks

Dielectric-metal-dielectric(DMD) electrode, which demonstrated excellent performances in terms of transparency, sheet resistance, and flexibility, is a promising approach towards flexible transparent electrodes[84]. Besides, the device performance can be remarkably improved by the microcavity effects with the DMD electrodes[84]. Xie et al.[85] fabricated the MoO$_3$/Ag/MoO$_3$ multilayer with a sheet resistance of 7 Ω/sq and an AVT of 73% and utilized it as the top transparent electrode for ST-PSCs. Besides, they found that the sheet resistance and AVT of DMD electrodes can be adjusted by modification of the deposition thickness and rate of Ag and WO$_3$. Similarly, Della Gaspera et al.[86] reported the use of MoO$_3$/Au/MoO$_3$ multilayer as a transparent electrode for MAPbI$_3$-based ST-PSCs, which achieved a record high PCE 13.6% with an AVT of 7%.

# 4 Prospect and Challenges

In this review, we provide a concise overview of the recent development in ST-PSCs for BIPV. Due to the rapid progress on its performance, stability, and environmental friendliness, as well as the excellent photoelectric properties and low-temperature fabrication methods, PVSK is considered as a promising photoactive material for ST-PV. The neutral colored ST-PSCs exhibit potential for fulfilling the strict requirements of dominated power generation windows installed in buildings or automobiles. In addition, the broad color tunability of PVSK offers possibilities of aesthetically appealing ST-PSCs. To further explore the potential of PVSK, here we offer our perspectives on the future directions for ST-PSCs.

**Table 1  Summary of ST-PSCs performance parameters(AVT is the average visible transmission values through the whole device, AL-AVT is the average visible transmission values of active layer)**

| Category | Feature | Device Strucure | Performance | | | | | | Ref. |
|---|---|---|---|---|---|---|---|---|---|
| | | | $J_{sc}$/(mA·cm$^{-2}$) | $V_{oc}$/V | FF(%) | PCE(%) | AL-AVT(%) | AVT(%) | |
| Large scale | Thin film | FTO/TiO$_2$/MAPbI$_{3-x}$Cl$_x$/Spiro-OMeTAD/ MoO$_3$/Ag | 16.2 | 1.06 | 0.49 | 8.5 | —— | —— | [26] |
| Graphene electrodes | Thin film | FTO/TiO$_2$/MAPbI$_{3-x}$Cl$_x$/Spiro-OMeTAD/ PEDOT:PS/Graphene(1 Layer) | 17.46 | 0.910 | 57.8 | 9.18 | —— | —— | [31] |
| | | FTO/TiO$_2$/MAPbI$_{3-x}$Cl$_x$/Spiro-OMeTAD/ PEDOT:PS/Graphene(2 Layers) | 19.17 | 0.960 | 67.22 | 12.37 | —— | —— | |
| | | FTO/TiO$_2$/MAPbI$_{3-x}$Cl$_x$/Spiro-OMeTAD/ PEDOT:PS/Graphene(3 Layers) | 18.54 | 0.940 | 65.70 | 11.45 | —— | —— | |
| | | FTO/TiO$_2$/MAPbI$_{3-x}$Cl$_x$/Spiro-OMeTAD/ PEDOT:PS/Graphene(4 Layers) | 18.05 | 0.950 | 65.72 | 11.27 | —— | —— | |
| Ultra-thin PVSK and Au electrode from evaporation | Thin film | ITO/PEDOT:PSS/MAPbI$_3$(40 nm)/ PCBM$_{60}$/Au/Lif | 5.66 | 1.037 | 57.7 | 3.39 | 45 | 35.4 | [38] |
| | | ITO/PEDOT:PSS/MAPbI$_3$(100 nm)/ PCBM$_{60}$/Au/Lif | 10.30 | 1.074 | 57.9 | 3.39 | 44 | 29 | |
| | | ITO/PEDOT:PSS/MAPbI$_3$(180 nm)/ PCBM$_{60}$/Au/Lif | 13.43 | 1.037 | 52.5 | 6.41 | 33 | 22 | |
| | | ITO/PEDOT:PSS/MAPbI$_3$(280 nm)/ PCBM$_{60}$/Au/Lif | 15.88 | 1.052 | 46.0 | 7.31 | 19 | 10 | |
| High $V_{oc}$ | Thin film | ITO/CuSCN/MAPbI$_3$(140 nm)/PCBM/ Bis-C$_{60}$/Ag | 9.15 | 1.070 | 75 | 7.33 | —— | 37.5 | [87] |
| | | ITO/CuSCN/MAPbI$_3$(180 nm)/PCBM/ Bis-C$_{60}$/Ag | 12.2 | 1.070 | 76 | 9.92 | —— | 25 | |
| | | ITO/CuSCN/MAPbI$_3$(240 nm)/PCBM/ Bis-C$_{60}$/Ag | 13.0 | 1.060 | 73 | 10.06 | —— | 13.0 | |
| Solution processable-transparent electrodes | Thin film | ITO/PEDOT:PSS/MAPbI$_{3-x}$Cl$_x$/PC$_{60}$BM/ Ag | 16.57 | 0.859 | 60.5 | 9.19 | 28.4 | —— | [28] |
| | | ITO/PEDOT:PSS/MAPbI$_{3-x}$Cl$_x$/PC$_{60}$BM/ ZnO/Ag | 15.46 | 0.945 | 71.9 | 10.68 | 28.4 | —— | |
| | | ITO/PEDOT:PSS/MAPbI$_{3-x}$Cl$_x$/PC$_{60}$BM/ ZnO/AgNWs | 13.13 | 0.964 | 66.8 | 8.49 | 28.4 | —— | |
| High $V_{oc}$ | Thin film | ITO/ZnO/CsPbBr$_3$/Spiro-OMeTAD/Au | 6.15 | 1.38 | 70.51 | 5.98 | —— | —— | [39] |
| Low scattering | Thin film | ITO/PEDOT:PSS/MAPbI$_3$(240 nm)/ PC$_{60}$BM/BCP/Ag | 16.6 | 1.02 | 64 | 10.66 | —— | —— | [33] |
| | | ITO/PEDOT:PSS/MAPbI$_3$(150 nm)/ PC$_{60}$BM/BCP/Ag | 11.08 | 0.98 | 0.61 | 6.87 | —— | —— | |
| Low scattering | Thin film | ITO/PC$_{71}$BM/MAPbI$_3$[(336±12) nm]/ Spiro-OMeTAD/MoO$_3$/Ag/MoO$_3$ | 14.97 | 0.904 | 48.96 | 6.76 | —— | 10.3 | [88] |
| | | ITO/PC$_{71}$BM/MAPbI$_3$[(247±18) nm]/ Spiro-OMeTAD/MoO$_3$/Ag/MoO$_3$ | 14.91 | 0.873 | 46.35 | 6.31 | —— | 10.6 | |
| | | ITO/PC$_{71}$BM/MAPbI$_3$[(160±16) nm]/ Spiro-OMeTAD/MoO$_3$/Ag/MoO$_3$ | 14.11 | 0.978 | 56.37 | 9.00 | —— | 10.7 | |
| | | ITO/PC$_{71}$BM/MAPbI$_3$[(138±9) nm]/ Spiro-OMeTAD/MoO$_3$/Ag/MoO$_3$ | 13.47 | 0.982 | 64.39 | 9.13 | —— | 12.4 | |
| | | ITO/PC$_{71}$BM/MAPbI$_3$[(93±12) nm]/ Spiro-OMeTAD/MoO$_3$/Ag/MoO$_3$ | 12.28 | 0.983 | 63.09 | 9.23 | —— | 14.1 | |
| | | ITO/PC$_{71}$BM/MAPbI$_3$[(50±9) nm]/ Spiro-OMeTAD/MoO$_3$/Ag/MoO$_3$ | 8.81 | 0.933 | 50.49 | 4.13 | —— | 17.5 | |
| | | ITO/PC$_{71}$BM/MAPbI$_3$[(45±7) nm]/ Spiro-OMeTAD/MoO$_3$/Ag/MoO$_3$ | 6.97 | 0.994 | 53.48 | 3.91 | —— | 19.0 | |
| | | ITO/PC$_{71}$BM/MAPbI$_3$[(40±12) nm]/ Spiro-OMeTAD/MoO$_3$/Ag/MoO$_3$ | 7.24 | 0.921 | 49.04 | 3.50 | —— | 20.5 | |
| Color-neutrality | Micro- | FTO/TiO$_2$/MAPbI$_3$ DVB(1%, molar fraction)/PTAA/PEDOT:PSS/ITO | 15.68 | 0.94 | 69.13 | 10.19 | —— | —— | [89] |
| | | FTO/TiO$_2$/MAPbI$_3$ DVB(3%, molar fraction)/PTAA/PEDOT:PSS/ITO | 16.20 | 0.97 | 70.59 | 11.09 | —— | —— | |
| | | FTO/TiO$_2$/MAPbI$_3$ DVB(5%, molar fraction)/PTAA/PEDOT:PSS/ITO | 16.52 | 0.98 | 73.79 | 11.95 | —— | —— | |
| | | FTO/TiO$_2$/MAPbI$_3$ DVB(7%, molar fraction)/PTAA/PEDOT:PSS/ITO | 16.33 | 0.97 | 71.58 | 11.46 | —— | —— | |

| Category | Feature | Device Strucure | Performance | | | | | | Ref. |
|---|---|---|---|---|---|---|---|---|---|
| | | | $J_{sc}$/(mA·cm$^{-2}$) | $V_{oc}$/V | FF(%) | PCE(%) | AL-AVT(%) | AVT(%) | |
| Color-neutrality | Micro- | FTO/TiO$_2$/MAPbI$_{3-x}$c$_x$/Spiro-OMeTAD/Au | 0.71 | 0.81 | 61 | 3.5 | 26.8 | — | [40] |
| Color-neutrality | Micro- | FTO/TiO$_2$/FAPbI$_3$/Spiro-OMeTAD/Au | 14.2 | 0.86 | 60 | 7.4 | 33.6 | — | [41] |
| | | FTO/TiO$_2$/MAPbI$_3$/Spiro-OMeTAD/Au | 10.6 | 0.64 | 54 | 4.9 | 40.5 | — | |
| Low-cost, large area | Ordered micro- | FTO/TiO$_2$/SiO$_2$·HC($n$=16) MAPbI$_{3-x}$Cl$_x$/ Spiro-OMeTAD/Ag | 17.1 | 0.84 | 66 | 9.5 | 37 | 28 | |
| | | FTO/TiO$_2$/Dewet($n$=11) MAPbI$_{3-x}$Cl$_x$/ Spiro-OMeTAD/Ag | 16.1 | 0.80 | 56 | 7.2 | 42 | 31 | |
| | | FTO/TiO$_2$/SiO$_2$·HC($n$=15) MA PbI$_{3-x}$Cl$_x$/ Spiro-OMeTAD/Ag | 7.6 | 0.80 | 74 | 4.5 | 63 | 47 | |
| | | FTO/TiO$_2$/Dewet($n$=10) MA PbI$_{3-x}$Cl$_x$/ Spiro-OMeTAD/Ag | 10.1 | 0.76 | 52 | 4.0 | 65 | 49 | |
| Color-neutrality | Ordered micro- | C-TiO$_2$/SiO$_2$ HC patterned MAPbI$_3$(10%, mass fraction)/Spiro-OMeTAD/Ag | 4.0 | 0.86 | 0.65 | 2.2 | 66 | 59 | [44] |
| | | C-TiO$_2$/SiO$_2$ HC patterned MAPbI$_3$(20%, mass fraction)/Spiro-OMeTAD/Ag | 11.9 | 0.89 | 0.53 | 6.2 | 40 | 36 | |
| | | C-TiO$_2$/SiO$_2$ HC patterned MAPbI$_3$(30%, mass fraction)/Spiro-OMeTAD/Ag | 16.5 | 0.98 | 0.56 | 9.1 | 38 | 34 | |
| | | C-TiO$_2$/SiO$_2$ HC patterned MAPbI$_3$(40%, mass fraction)/Spiro-OMeTAD/Ag | 17.5 | 0.98 | 0.56 | 9.8 | 17 | 15 | |
| Color neutrality, robust | Nano- | FTO/TiO$_2$/AAO+MAPbI$_{3-x}$Cl$_x$(400 nm)/ Spiro-OMeTAD/Au | 20.24 | 1.03 | 76 | 15.78 | — | — | [52] |
| | | FTO/TiO$_2$/AAO+MAPbI$_{3-x}$Cl$_x$(290 nm)/ Spiro-OMeTAD/Au | 15.38 | 1.02 | 75.48 | 11.81 | — | — | |
| | | FTO/TiO$_2$/AAO+MAPbI$_{3-x}$Cl$_x$(170 nm)/ Spiro-OMeTAD/Au | 14.39 | 1.01 | 74.49 | 10.86 | — | — | |
| | | FTO/TiO$_2$/AAO+MAPbI$_{3-x}$Cl$_x$(100 nm)/ Spiro-OMeTAD/Au | 12.64 | 0.96 | 74 | 8.98 | — | — | |
| | | FTO/TiO$_2$/AAO+MAPbI$_3$(70 nm)/ Spiro-OMeTAD/Au | 12.24 | 0.92 | 70.52 | 7.91 | — | — | |
| | | FTO/TiO$_2$/AAO(90 nm)+MAPbI$_{3-x}$Cl$_x$ (150 nm)/Spiro-OMeTAD/Au | 12.06 | 0.96 | 73.48 | 8.49 | — | 45.4 | |
| | | FTO/TiO$_2$/AAO(150 nm)+ MAPbI$_{3-x}$Cl$_x$ (220 nm)/Spiro-OMeTAD/Au | 13.58 | 1 | 75.08 | 10.26 | — | 41.5 | |
| | | FTO/TiO$_2$/AAO(220 nm)+ MAPbI$_{3-x}$Cl$_x$ (300 nm)/Spiro-OMeTAD/Au | 14.67 | 1.01 | 73.1 | 10.81 | — | 37.4 | |
| | | FTO/TiO$_2$/AAO(280 nm)+MAPbI$_{3-x}$Cl$_x$ (350 nm)/Spiro-OMeTAD/Au | 15.87 | 0.99 | 74.53 | 11.72 | — | 33.5 | |
| | | FTO/TiO$_2$/AAO(340 nm)+MAPbI$_{3-x}$Cl$_x$ (440 nm)/Spiro-OMeTAD/Au | 16.54 | 1.03 | 74.69 | 12.77 | — | 29.8 | |
| | | FTO/TiO$_2$/AAO(460 nm)+MAPbI$_{3-x}$Cl$_x$ (610 nm)/Spiro-OMeTAD/Au | 17.72 | 1.03 | 72.38 | 13.27 | — | 26.3 | |
| Human luminosity | Nano- | ITO/PEDOT:PSS/MAPbI$_3$(180 nm)/ PCBM/Ag NCs/BCP/Ag/MoO$_3$ | 15.69 | 1.02 | 60 | 9.73 | — | 17.8 | [47] |
| | | ITO/PEDOT:PSS/MAPbI$_3$(180 nm)/PCBM | 13.48 | 1.02 | 61 | 8.62 | — | 19.8 | |
| | | ITO/PEDOT:PSS/MAPbI$_3$(210 nm)/PCBM | 15.34 | 1.00 | 60 | 9.18 | — | 15.2 | |

To achieve efficient and high visually transparent ST-PSCs, it is highly desired to tune the absorption spectrum of ST-PSCs to the near-infrared and ultraviolet region instead of the visible range in the solar spectrum. Besides, by absorbing near-infrared radiation, the power generation windows provide shading of buildings during the day, which will reduce the electricity cost for cooling and heating. One possible approach towards the high near-infrared absorbing ST-PV is the tandem device of PVSK and low bandgap organic semiconductors. Moreover, the ultraviolet absorption from the PVSK is beneficial to prevent the undesired effects come along with ultraviolet light, such as the aging of furniture or portrayals. Thus the ST-PSCs have the potential to be a smart product that can combine with power-generating, heat preservation, and ultraviolet blocking.

On the other hand, a cost-effective method to fabricate large scale solar cell is the prerequisite for commercialization. Moreover, architecture aesthetics do matter. The flexibility of a solar cell is essential if we want to combine with the solar cell with membrane architecture. Therefore, the light-weight bendable ST-PSCs, which can be fabricated through the continued roll-to-roll process, will be promising products in the future.

Notably, the long-term stability and toxicity of PVSK need to be solved before commercialization. Recent works have shown that the toxicity issue can be mitigated by replacing Pb with Sn, Bi, Ag, or other metals partially or entirely. However, a drop in efficiency occurs as the concentration of lead decreases, which needs to be tackled in future work. Also, importantly, even though the lifetime of PSCs has been remarkably

enhanced from a few minutes to >10000 hours, for viable commercial products, the lifetime should be substantially improved to 10 years or even longer.

## References

[1] 2019-Snapshot of Global Photovoltaic Markets, https://www.researchgate.net/publication/332606669

[2] File M., *Commercial Buildings Energy Consumption Survey* (*CBECS*), https://www.eia.gov/consumption/commercial/data/2012/

[3] Werner J. R. M., Barraud L., Walter A., Bräuninger M., Sahli F., Sacchetto D., Tétreault N., Paviet-Salomon B., Moon S. J., Allebé C., *ACS Energy Letters,* **2016**, *1*(2), 474

[4] Gagnon P., Margolis R., Phillips C., *Rooftop Photovoltaic Technical Potential in the United States*; National Renewable Energy Laboratory-Data(NREL-DATA), Golden, CO(United States: 2019), https://www.nrel.gov/docs/fy16osti/65298.pdf

[5] US Energy Information Adminstration, *2015 Residential Energy Consumption Survey(RECS) Data*, **2015**, https://www.eia.gov/consumption/residential/data/2015/

[6] Zhao D., Yu Y., Wang C., Liao W., Shrestha N., Grice C. R., Cimaroli A. J., Guan L., Ellingson R. J., Zhu K., *Nature Energy*, **2017**, *2*(4), 17018

[7] Zhu Y., Poddar S., Shu L., Fu Y., Fan Z., *Advanced Materials Interfaces*, **2020**, 2000118

[8] National Renewable Energy Laboratory, *Best Research Cell Efficiencies Chart*, **2019**, https://www.nrel.gov/pv/cell-efficiency.html

[9] Wang R., Mujahid M., Duan Y., Wang Z. K., Xue J., Yang Y., *Advanced Functional Materials*, **2019**, *29*(47), 1808843

[10] Grancini G., Roldán-Carmona C., Zimmermann I., Mosconi E., Lee X., Martineau D., Narbey S., Oswald F., De Angelis F., Graetzel M., *Nature Communications*, **2017**, *8*, 15684

[11] McMeekin D. P., Sadoughi G., Rehman W., Eperon G. E., Saliba M., Hörantner M. T., Haghighirad A., Sakai N., Korte L., Rech B., *Science*, **2016**, *351*(6269), 151

[12] Noh J. H., Im S. H., Heo J. H., Mandal T. N., Seok S. I., *Nano Letters*, **2013**, *13*(4), 1764

[13] Eperon G. E., Stranks S. D., Menelaou C., Johnston M. B., Herz L. M., Snaith H. J., *Energy & Environmental Science*, **2014**, *7*(3), 982

[14] Judd D. B., *Contributions to Color Science*, Department of Commerce, National Bureau of Standards, **1979**

[15] Traverse C. J., Pandey R., Barr M. C., Lunt R. R., *Nature Energy*, **2017**, *2*(11), 849

[16] Drolet N., *Organic Photovoltaic: Efficiency and Lifetime Challenges for Commercial Viability, 2012 MRS Spring Meeting & Exhibit*, Moscone West Convention Center, Marriott Marquis San Francisco, CA, **2012**

[17] Poynton C., *Digital Video and HD: Algorithms and Interfaces*, Elsevier, Waltham MA, **2012**

[18] Deng Y., Wang Q., Yuan Y., Huang J., *Materials Horizons*, **2015**, *2*(6), 578

[19] Zhang W., Anaya M., Lozano G., Calvo M. E., Johnston M. B., Míguez H., Snaith H. J., *Nano Letters*, **2015**, *15*(3), 1698

[20] Lee K. T., Jang J. Y., Zhang J., Yang S. M., Park S., Park H. J., *Scientific Reports*, **2017**, *7*(1), 1

[21] Schlisske S ., Mathies F ., Busko D ., Strobel N ., Rödlmeier T ., Richards B. S., Lemmer U., Paetzold U. W., Hernandez-Sosa G., Klampaftis E., *ACS Applied Energy Materials*, **2018**, *2*(1), 764

[22] Beal R. E., Slotcavage D. J., Leijtens T., Bowring A. R., Belisle R. A., Nguyen W. H., Burkhard G. F., Hoke E. T., McGehee M. D., *The Journal of Physical Chemistry Letters*, **2016**, *7*(5), 746

[23] McMeekin D. P., Sadoughi G., Rehman W., Eperon G. E., Saliba M., Hörantner M. T., Haghighirad A., Sakai N., Korte L., Rech B. J. S., **2016**, *351*(6269), 151

[24] Lee J. W., Kim D. H., Kim H. S., Seo S. W., Cho S. M., Park N. G., *Advanced Energy Materials*, **2015**, *5*(20), 1501310

[25] You P., Liu Z., Tai Q., Liu S., Yan F., *Advanced Materials*, **2015**, *27*(24), 3632

[26] Ono L. K., Wang S., Kato Y., Raga S. R., Qi Y., *Energy & Environmental Science*, **2014**, *7*(12), 3989

[27] Jung J. W., Chueh C. C., Jen A. K. Y., *Advanced Energy Materials*, **2015**, *5*(17), 1500486

[28] Guo F., Azimi H., Hou Y., Przybilla T., Hu M., Bronnbauer C., Langner S., Spiecker E., Forberich K., Brabec C. J., *Nanoscale*, **2015**, *7*(5), 1642

[29] Heo J. H., Han H. J., Lee M., Song M., Kim D. H., Im S. H., *Energy & Environmental Science*, **2015**, *8*(10), 2922

[30] Quiroz C. O. R., Levchuk I., Bronnbauer C., Salvador M., Forberich K., Heumüller T., Hou Y., Schweizer P., Spiecker E., Brabec C. J., *Journal of Materials Chemistry A*, **2015**, *3*(47), 24071

[31] You P., Liu Z., Tai Q., Liu S., Yan F. J. A. M., **2015**, *27*(24), 3632

[32] Kim Y. C., Jeon N. J., Noh J. H., Yang W. S., Seo J., Yun J. S., Ho-Baillie A., Huang S., Green M. A., Seidel J., *Advanced Energy Materials*, **2016**, *6*(4), 1502104

[33] Kim G. M., Tatsuma T., *The Journal of Physical Chemistry C*, **2016**, *120*(51), 28933

[34] Kam M., Zhang Q., Zhang D., Fan Z., *Scientific Reports*, **2019**, *9*(1), 1

[35] Kam M., Zhu Y., Zhang D., Gu L., Chen J., Fan Z., *Solar RRL*, **2019**, *3*(7), 1900050

[36] Tavakoli M. M., Lin Q., Leung S. F., Lui G. C., Lu H., Li L., Xiang B., Fan Z., *Nanoscale*, **2016**, *8*(7), 4276

[37] Tavakoli M. M., Simchi A., Mo X., Fan Z., *Materials Chemistry Frontiers*, **2017**, *1*(8), 1520

[38] Roldán-Carmona C., Malinkiewicz O., Betancur R., Longo G., Momblona C., Jaramillo F., Camacho L., Bolink H. J. J. E., *Science E.*, **2014**, *7*(9), 2968

[39] Chen W., Zhang J., Xu G., Xue R., Li Y., Zhou Y., Hou J., Li Y., *Advanced Materials*, **2018**, *30*(21), 1800855

[40] Eperon G. E., Burlakov V. M., Goriely A., Snaith H. J., *ACS Nano*, **2013**, *8*(1), 591

[41] Eperon G. E., Bryant D., Troughton J., Stranks S. D., Johnston M. B., Watson T., Worsley D. A., Snaith H. J., *The Journal of Physical Chemistry Letters*, **2015**, *6*(1), 129

[42] Della Gaspera E., Peng Y., Hou Q., Spiccia L., Bach U., Jasieniak J. J., Cheng Y. B., *Nano Energy*, **2015**, *13*, 249

[43] Hörantner M., Zhang W., Saliba M., Wojciechowski K., Snaith H., *Energy & Environmental Science*, **2015**, *8*(7), 2041

[44] Zhang L., Hörantner M. T., Zhang W., Yan Q., Snaith H. J., *Solar Energy Materials and Solar Cells*, **2017**, *160*, 193

[45] Retsch M., Zhou Z., Rivera S., Kappl M., Zhao X. S., Jonas U., Li Q., *Macromolecular Chemistry and Physics*, **2009**, *210*(3/4), 230

[46] Plettl A., Enderle F., Saitner M., Manzke A., Pfahler C., Wiedemann S., Ziemann P., *Advanced Functional Materials*, **2009**, *19*(20), 3279

[47] Kim G. M., Tatsuma T., *Scientific Reports*, **2017**, *7*(1), 10699

[48] Zhang D., Gu L., Zhang Q., Lin Y., Lien D. H., Kam M., Poddar S.,

Garnett E. C., Javey A., Fan Z., *Nano Letters*, **2019**, *19*(5), 2850

[49] Gu L., Zhang D., Kam M., Zhang Q., Poddar S., Fu Y., Mo X., Fan Z., *Nanoscale*, **2018**, *10*(32), 15164

[50] Zhang Q., Zhang D., Gu L., Tsui K. H., Poddar S., Fu Y., Shu L., Fan Z., *ACS Nano*, **2020**

[51] Zhang Q., Tavakoli M. M., Gu L., Zhang D., Tang L., Gao Y., Guo J., Lin Y., Leung S. F., Poddar S., *Nature Communications*, **2019**, *10*(1), 1

[52] Kwon H. C., Kim A., Lee H., Lee D., Jeong S., J. Moon J., *Adv. Energy Mater.*, **2016**, *6*(20), 1601055

[53] Kawawaki T., Takahashi Y., Tatsuma T., *Nanoscale*, **2011**, *3*(7), 2865

[54] Stuart H. R., Hall D. G., *Applied Physics Letters*, **1998**, *73*(26), 3815

[55] Stenzel O., Stendal A., Voigtsberger K., Von Borczyskowski C., *Solar Energy Materials and Solar Cells*, **1995**, *37*(3/4), 337

[56] Wei Z., Smith B., De Rossi F., Searle J. R., Worsley D. A., Watson T. M., *Journal of Materials Chemistry C*, **2019**, *7*(35), 10981

[57] Bryant D., Greenwood P., Troughton J., Wijdekop M., Carnie M., Davies M., Wojciechowski K., Snaith H. J., Watson T., Worsley D., *Advanced Materials*, **2014**, *26*(44), 7499

[58] Fu F., Feurer T., Jäger T., Avancini E., Bissig B., Yoon S., Buecheler S., Tiwari A. N., *Nature Communications*, **2015**, *6*(1), 1

[59] Werner J., Dubuis G., Walter A., Löper P., Moon S. J., Nicolay S., Morales-Masis M., De Wolf S., Niesen B., Ballif C. J. S. E. M., Cells S., **2015**, *141*, 407

[60] Wahl T., Hanisch J., Meier S., Schultes M., Ahlswede E., *Organic Electronics*, **2018**, *54*, 48

[61] Chiang Y. H., Peng C. C., Chen Y. H., Tung Y. L., Tsai S. Y., Chen P., *Journal of Physics D: Applied Physics*, **2018**, *51*(42), 424002

[62] Fu F., Pisoni S., Weiss T. P., Feurer T., Wäckerlin A., Fuchs P., Nishiwaki S., Zortea L., Tiwari A. N., *Efficient and Stable Nir-Transparent Perovskite Solar Cells for Thin-Film Tandem Photovoltaics*, **2017**, 115

[63] Bush K. A., Bailie C. D., Chen Y., Bowring A. R., Wang W., Ma W., Leijtens T., Moghadam F., McGehee M. D., *Advanced Materials*, **2016**, *28*(20), 3937

[64] Acik M., Darling S. B., *Journal of Materials Chemistry A*, **2016**, *4*(17), 6185

[65] Bailie C. D., Christoforo M. G., Mailoa J. P., Bowring A. R., Unger E. L., Nguyen W. H., Burschka J., Pellet N., Lee J. Z., Grätzel M., *Energy & Environmental Science*, **2015**, *8*(3), 956

[66] Hellstrom S. L., Vosgueritchian M., Stoltenberg R. M., Irfan I., Hammock M., Wang Y. B., Jia C., Guo X., Gao Y., Bao Z., *Nano Letters*, **2012**, *12*(7), 3574

[67] Lang F., Gluba M. A., Albrecht S., Rappich J. R., Korte L., Rech B., Nickel N. H., *The Journal of Physical Chemistry Letters*, **2015**, *6*(14), 2745

[68] Hecht D. S., Hu L., Irvin G., *Advanced Materials*, **2011**, *23*(13), 1482

[69] Yu Z., Li L., Zhang Q., Hu W., Pei Q., *Advanced Materials*, **2011**, *23*(38), 4453

[70] Yang Y., Chen Q., Hsieh Y. T., Song T. B., Marco N. D., Zhou H., Yang Y., *ACS Nano*, **2015**, *9*(7), 7714

[71] Bae S., Kim H., Lee Y., Xu X., Park J. S., Zheng Y., Balakrishnan J., Lei T., Kim H. R., Song Y. I., *Nature Nanotechnology*, **2010**, *5*(8), 574

[72] Kim K. S., Zhao Y., Jang H., Lee S. Y., Kim J. M., Kim K. S., Ahn J. H., Kim P., Choi J. Y., Hong B. H., *Nature*, **2009**, *457*(7230), 706

[73] Tan R. K. L., Reeves S. P., Hashemi N., Thomas D. G., Kavak E., Montazami R., Hashemi N. N., *Journal of Materials Chemistry A*, **2017**, *5*(34), 17777

[74] Geim A. K., Novoselov K. S., *Nanoscience and Technology: a Collection of Reviews from Nature Journals*, World Scientific, Singapore, **2010**, 11

[75] Tran V. D., Pammi S., Park B. J., Han Y., Jeon C., Yoon S. G., *Nano Energy*, **2019**, *65*, 104018

[76] Lee B. H., Lee J. H., Kahng Y. H., Kim N., Kim Y. J., Lee J., Lee T., Lee K., *Advanced Functional Materials*, **2014**, *24*(13), 1847

[77] Li Z., Kulkarni S. A., Boix P. P., Shi E., Cao A., Fu K., Batabyal S. K., Zhang J., Xiong Q., Wong L. H., *ACS Nano*, **2014**, *8*(7), 6797

[78] Bonaccorso F., Sun Z., Hasan T., Ferrari A., *Nature Photonics*, **2010**, *4*(9), 611

[79] Ginley D. S., Hosono H., Paine D. C., **2010**

[80] Guo F., Azimi H., Hou Y., Przybilla T., Hu M., Bronnbauer C., Langner S., Spiecker E., Forberich K., Brabec C. J., *Nanoscale*, **2015**, *7*(5), 1642

[81] Lee H. S., Kim Y. W., Kim J. E., Yoon S. W., Kim T. Y., Noh J. S., Suh K. S., *Acta Materialia*, **2015**, *83*, 84

[82] Zhao W., Gan X., Ke L., Guo L., Liu H., *Solar Energy*, **2020**, *196*, 1

[83] Han K., Xie M., Zhang L., Yan L., Wei J., Ji G., Luo Q., Lin J., Hao Y., Ma C. Q., *Solar Energy Materials and Solar Cells*, **2018**, *185*, 399

[84] Kim S., Lee J. L., *Journal of Photonics for Energy*, **2012**, *2*(1), 021215

[85] Xie X., Wu C., Sun S., Xu X., Xu W., Qin G., Xiao L., *Energy Technology*, **2019**, 1900868

[86] Della Gaspera E., Peng Y., Hou Q., Spiccia L., Bach U., Jasieniak J. J., Cheng Y. B., *Nano Energy*, **2015**, *13*, 249

[87] Jung J. W., Chueh C. C., Jen A. K. Y., *Adv. Energy Mater.*, **2015**, *5*(17), 1500486

[88] Upama M. B., Mahmud M. A., Yi H., Elumalai N. K., Conibeer G., Wang D., Xu C., Uddin A., *Organic Electronics*, **2019**, *65*, 401

[89] Heo J. H., Han J., Shin D. H., Im S. H., *Materials Today Energy*, **2017**, *5*, 280